

Creation of a longitudinally polarized subwavelength hotspot with an ultra-thin planar lens:
vectorial Rayleigh–Sommerfeld method

This article has been downloaded from IOPscience. Please scroll down to see the full text article.

2013 Laser Phys. Lett. 10 065004

(<http://iopscience.iop.org/1612-202X/10/6/065004>)

View [the table of contents for this issue](#), or go to the [journal homepage](#) for more

Download details:

IP Address: 137.132.3.9

The article was downloaded on 09/05/2013 at 01:51

Please note that [terms and conditions apply](#).

LETTER

Creation of a longitudinally polarized subwavelength hotspot with an ultra-thin planar lens: vectorial Rayleigh–Sommerfeld method

Huapeng Ye¹, Cheng-Wei Qiu¹, Kun Huang¹, Jinghua Teng², Boris Luk'yanchuk³ and Swee Ping Yeo¹

¹ Department of Electrical and Computer Engineering, National University of Singapore, 117583, Singapore

² Institute of Materials Research and Engineering, Agency for Science, Technology and Research, 3 Research Link, Singapore 117602, Singapore

³ Data Storage Institute, Agency for Science, Technology and Research, 5 Engineering Drive 1, Singapore 117608, Singapore

E-mail: chengwei.qiu@nus.edu.sg

Received 4 February 2013, in final form 19 February 2013

Accepted for publication 22 February 2013

Published 8 May 2013

Online at stacks.iop.org/LPL/10/065004

Abstract

This letter shows how a longitudinally polarized hotspot can be created by a planar ultra-thin lens that beats the diffraction limit. On the imaging plane, a subwavelength optical resolution 0.39λ with almost purely longitudinal electric component has been demonstrated in air ambient. This novel paradigm addresses simultaneously both longitudinal polarization and deep sub-diffraction imaging, by a planar lens composed of ultra-thin opaque concentric annuli. The vectorial Rayleigh–Sommerfeld (VRS) approach, offering the advantage of significant reduction in computation, has been developed for a particular optimization of a flat lens with full control of polarization. Empowered by the robustness of VRS in dealing with polarization states, the proposed roadmap may be universally and efficiently integrated with other optimization algorithms to design super-resolution imaging with controlled polarization states at any wavelength without luminescence of the object. The lens, which is empowered by the proposed method, opens an avenue for the first time toward a highly integrated imaging system with advanced functionalities in far-field super-imaging, tailored polarization states and flat ultra-thin geometry simultaneously.

(Some figures may appear in colour only in the online journal)

1. Introduction

Diffraction, which occurs naturally when a wave encounters an obstacle, is a fundamental feature that affects imaging systems such as cameras, telescopes and microscopes [1–3].

The analysis of light diffraction usually entails the direct or approximate calculation of diffraction integrals [4–8]. Traditionally, a rule of thumb when choosing between scalar integrals and vectorial integrals is to consider the numerical aperture (NA) of the lens used for light focusing: scalar theory

is known to yield accurate predictions when the NA is smaller than approximately 0.7 [8]. However, it has to be borne in mind that unpolarized light becomes fully polarized in the focal region when using high-NA focusing [9]. In general, calculations based on scalar theory tend to underestimate the hotspot size when the NA is no longer small [10], as the vectorial properties of incident light not only affect the local field direction but also the intensity distribution at the focus. In fact, the simulation results reported in [11] indicate that the hotspot derived from scalar theory is larger than that computed by vectorial theory or numerical algorithms even when the NA is as small as 0.25. This is particularly important when attempting to achieve far-field hotspots beyond the diffraction limit, such as in super-resolution imaging, high-density data storage or 3D lithography [3, 12].

On the other hand, the intensity and vectorial properties of the incident light also affect the interaction with materials [13, 14]. Light with a strong longitudinal electric-field component tends to create an ablation crater at the focal region and minimize the cracks generated by transverse components, thus helping to smoothen the interface [15, 16]; this has been applied in data recording on phase-change materials [17–20]. Traditionally, a strong and tight longitudinal electric field is realized by a high-NA lens together with a circular or angular aperture [10, 21]. It can also be created by lens-assisted and phase-controlled binary optics [22].

Recently, the diffraction-based super-oscillatory lens [3, 23] has been experimentally shown to yield super-resolution [24, 25]. The planar diffraction-based lens [3, 23] has many advantages, i.e., no physical limits on resolution (but at the expense of a larger sidelobe), relatively easy implementation and working in the far-field. Apart from the huge-sidelobe problem, which is inevitable owing to super-oscillation theory, such a super-resolution hotspot is in the far-field of the lens and requires a number of optimized ring structures. Hence, the conventional scalar method or finite difference time domain (FDTD)-based commercial software will manifest severe accuracy problems or computational difficulties which in turn prohibit robust optimization for the super-resolution lens. The situation becomes even more challenging when we need to consider specially polarized incident light, e.g., radially or azimuthally polarized light.

In order to proceed, we must make recourse to a robust version of vectorial diffraction theory which can serve as a fundamental, rigorous and highly efficient method used in this letter to design and optimize the flat diffraction lens to achieve a subwavelength and even super-resolution hotspot in the far-field. Moreover, the polarization state of the hotspot can be fully designed and manipulated at will. As an example of what is feasible, we have demonstrated the design of a flat diffraction lens with a deep subwavelength hotspot (0.39λ) of almost 100% longitudinal electric component in the far-field imaging center. To analyze this flat lens composed of dozens of concentric rings, we have adopted the proposed vectorial Rayleigh–Sommerfeld (VRS) integral method in conjunction with binary particle swarm optimization [26]. Our

simulations show good agreement between the analytical VRS results and the numerical data computed by FDTD (Lumerical Solutions Corp. [27]) with the advantage of markedly reduced computational resources required by our far-field and optimization algorithms. Another advantage of using VRS is that a three-dimensional (3D) problem may be conveniently simplified into a 2D or even 1D problem along the optical axis by virtue of axial symmetry, thereby drastically reducing the computational time taken during the design of an optimized lens with lower noise level, broader field of view and smaller hotspot size. These advantages in turn become significant when the optimization algorithm is employed to search for a flat diffraction lens for super-resolution hotspots.

2. Vectorial Rayleigh–Sommerfeld integral

The first-kind Rayleigh–Sommerfeld diffraction integrals may be written in the following form [28]:

$$E_x(u, v, z) = -\frac{1}{2\pi} \iint_{R^2} E_x(x, y, 0) \frac{\partial}{\partial z} \left[\frac{\exp(iknR)}{R} \right] dx dy \quad (1a)$$

$$E_y(u, v, z) = -\frac{1}{2\pi} \iint_{R^2} E_y(x, y, 0) \frac{\partial}{\partial z} \left[\frac{\exp(iknR)}{R} \right] dx dy \quad (1b)$$

$$E_z(u, v, z) = \frac{1}{2\pi} \iint_{R^2} \left\{ E_x(x, y, 0) \frac{\partial}{\partial u} \left[\frac{\exp(iknR)}{R} \right] + E_y(x, y, 0) \frac{\partial}{\partial v} \left[\frac{\exp(iknR)}{R} \right] \right\} dx dy \quad (1c)$$

where $R^2 = z^2 + (x - u)^2 + (y - v)^2$; $E_x(x, y, 0)$ and $E_y(x, y, 0)$ denote the electric-field components along the x and y directions, respectively; n is the refractive index of the medium space; $(x, y, 0)$ and (u, v, z) represent the incident and observation planes, respectively. Solution of the differentials in equation (1) provides us with simplified forms of the first-kind VRS formulas expressed in Cartesian coordinates,

$$E_x(u, v, z) = -\frac{1}{2\pi} \iint_{R^2} E_x(x, y, 0) \times \left[\frac{z \exp(iknR)}{R^2} \left(ikn - \frac{1}{R} \right) \right] dx dy \quad (2a)$$

$$E_y(u, v, z) = -\frac{1}{2\pi} \iint_{R^2} E_y(x, y, 0) \times \left[\frac{z \exp(iknR)}{R^2} \left(ikn - \frac{1}{R} \right) \right] dx dy \quad (2b)$$

$$E_z(u, v, z) = \frac{1}{2\pi} \iint_{R^2} \left[\frac{\exp(iknR)}{R^2} \left(\frac{1}{R} - ikn \right) \right] \times [E_x(x, y, 0)(x - u) + E_y(x, y, 0)(y - v)] dx dy. \quad (2c)$$

To transform these electric-field components along the Cartesian-coordinate axes into their cylindrical-coordinate counterparts, we need to employ the following equation, with $(r, \varphi, 0)$ and (ρ, θ, z) now representing the incident and

observation planes, respectively:

$$\begin{bmatrix} E_r \\ E_\varphi \end{bmatrix} = \begin{bmatrix} \cos \varphi & \sin \varphi \\ -\sin \varphi & \cos \varphi \end{bmatrix} \cdot \begin{bmatrix} E_x \\ E_y \end{bmatrix} \quad (3)$$

where $\cos \varphi = \frac{x}{\sqrt{x^2+y^2}}$, $\sin \varphi = \frac{y}{\sqrt{x^2+y^2}}$.

The radial, azimuthal and longitudinal components may then be written in cylindrical coordinates as

$$E_r(\rho, \theta, z) = -\frac{1}{2\pi} \iint_{R^2} [E_r(r, \varphi, 0) \cos(\varphi - \theta) - E_\varphi(r, \varphi, 0) \sin(\varphi - \theta)] \frac{\partial}{\partial z} \left[\frac{\exp(iknR)}{R} \right] r dr d\varphi \quad (4a)$$

$$E_\varphi(\rho, \theta, z) = -\frac{1}{2\pi} \iint_{R^2} [E_\varphi(r, \varphi, 0) \cos(\varphi - \theta) + E_r(r, \varphi, 0) \sin(\varphi - \theta)] \frac{\partial}{\partial z} \left[\frac{\exp(iknR)}{R} \right] r dr d\varphi \quad (4b)$$

$$E_z(\rho, \theta, z) = \frac{1}{2\pi} \iint_{R^2} \{E_r(r, \varphi, 0)[r - \rho \cos(\varphi - \theta)] + E_\varphi(r, \varphi, 0)\rho \sin(\varphi - \theta)\} \frac{1}{R} \frac{\partial}{\partial R} \left[\frac{\exp(iknR)}{R} \right] r dr d\varphi \quad (4c)$$

where $R^2 = z^2 + \rho^2 + r^2 - 2\rho r \cos(\varphi - \theta)$. Equation (4) thus allows us to obtain the following expressions for the requisite field components:

$$E_r(\rho, \theta, z) = -\frac{1}{2\pi} \iint_{R^2} [E_r(r, \varphi, 0) \cos(\varphi - \theta) - E_\varphi(r, \varphi, 0) \sin(\varphi - \theta)] \left(ikn - \frac{1}{R} \right) \times \left[\frac{z}{R^2} \exp(iknR) \right] r dr d\varphi \quad (5a)$$

$$E_\varphi(\rho, \theta, z) = -\frac{1}{2\pi} \iint_{R^2} [E_\varphi(r, \varphi, 0) \cos(\varphi - \theta) + E_r(r, \varphi, 0) \sin(\varphi - \theta)] \left(ikn - \frac{1}{R} \right) \times \left[\frac{z}{R^2} \exp(iknR) \right] r dr d\varphi \quad (5b)$$

$$E_z(\rho, \theta, z) = \frac{1}{2\pi} \iint_{R^2} \{E_r(r, \varphi, 0)[r - \rho \cos(\varphi - \theta)] + E_\varphi(r, \varphi, 0)\rho \sin(\varphi - \theta)\} \frac{\exp(iknR)}{R^2} \times \left(ikn - \frac{1}{R} \right) r dr d\varphi. \quad (5c)$$

Since the integration with respect to the cylindrical-coordinate variable φ yields a nil result, we infer that equation (5) can be further simplified in the following manner:

$$\begin{aligned} & \int_0^{2\pi} \sin(\varphi - \theta) \frac{\partial}{\partial z} \left[\frac{\exp(iknR)}{R} \right] d\varphi \\ &= - \int_0^{2\pi} \frac{\partial}{\partial z} \left[\frac{\exp(iknR)}{R} \right] d \cos(\varphi - \theta) \\ &= -\psi[\cos(\varphi - \theta)] = 0 \end{aligned}$$

where ψ is the anti-derivative of the following function:

$$\frac{\partial}{\partial z} \left[\frac{\exp(ikn\sqrt{z^2 + \rho^2 + r^2 - 2\rho r \cos(\varphi - \theta)})}{\sqrt{z^2 + \rho^2 + r^2 - 2\rho r \cos(\varphi - \theta)}} \right].$$

Finally, we have the simplified forms of these VRS formulas expressed in cylindrical coordinates as

$$E_r(\rho, \theta, z) = -\frac{1}{2\pi} \iint_{R^2} [E_r(r, \varphi, 0) \cos(\varphi - \theta)] \times \left(ikn - \frac{1}{R} \right) \left[\frac{z}{R^2} \exp(iknR) \right] r dr d\varphi \quad (6a)$$

$$E_\varphi(\rho, \theta, z) = -\frac{1}{2\pi} \iint_{R^2} [E_\varphi(r, \varphi, 0) \cos(\varphi - \theta)] \times \left(ikn - \frac{1}{R} \right) \left[\frac{z}{R^2} \exp(iknR) \right] r dr d\varphi \quad (6b)$$

$$E_z(\rho, \theta, z) = \frac{1}{2\pi} \iint_{R^2} E_r(r, \varphi, 0)[r - \rho \cos(\varphi - \theta)] \times \frac{\exp(iknR)}{R^2} \left(ikn - \frac{1}{R} \right) r dr d\varphi. \quad (6c)$$

If the field has radial symmetry (whether radially or azimuthally polarized) in the original plane, we infer from equation (6) that it will retain its (radial or azimuthal) polarization during propagation.

3. Results and discussion

In this letter, air is presumed to be the ambient medium throughout. To demonstrate the validity of employing first-kind VRS in the design and optimization of a planar diffraction-based lens composed of concentric annuli, we have chosen to include FDTD verification when studying the diffraction of the circular apertures. For the first-kind VRS given by equations (2a)–(2c) in Cartesian coordinates, we have conveniently selected a wavelength of $\lambda = 640$ nm for our numerical simulations with the incident electric field normalized to $E = 1$ (i.e., unit incident field). For FDTD, a linearly polarized plane wave with the same wavelength of 640 nm as that adopted in VRS is incident onto an aperture inside a 200 nm thick aluminum film. Figure 1 shows the E -field intensity distribution plots along the optical axis generated by both VRS and 3D FDTD for various values of the aperture diameter D . When D is very small, the field decays rapidly, as depicted in figures 1(a)–(c), because diffraction is always accompanied by divergence; the smaller the aperture is, the faster the light will diverge [29, 30]. In addition, it is evident from figures 1(d)–(f) that there is good agreement between the plots generated by VRS and FDTD for the E -field intensity distribution along the optical axis in both intermediate- and far-field when the lateral dimension of the circular aperture exceeds 5 wavelengths.

To further illustrate this, the E -field intensity distribution in the plane perpendicular to the longitudinal direction $6.5 \mu\text{m}$ away from the alumina thin film is shown in figure 2, where the aperture diameter is fixed at 5 wavelengths. For simplicity, we have adopted linearly polarized light along the x direction for both VRS and FDTD in order to capitalize

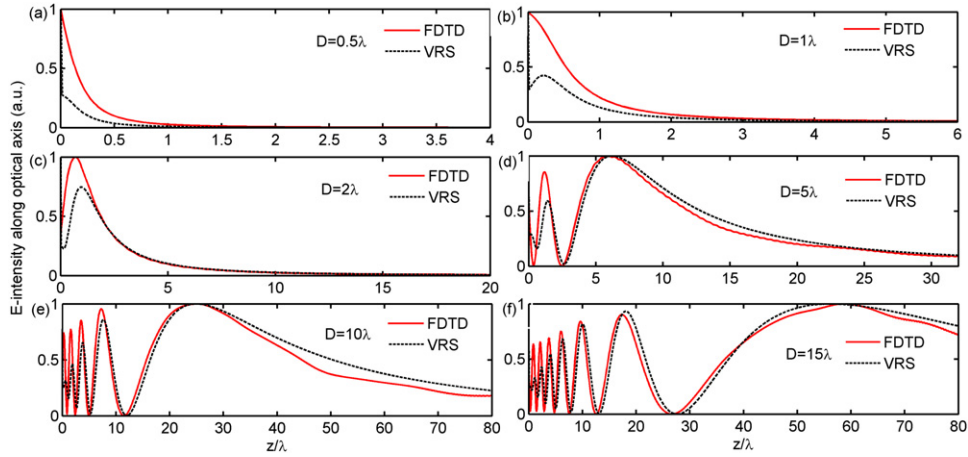


Figure 1. (a)–(f) E -field intensity along the optical axis computed by Lumerical FDTD and VRS where incident light is linearly polarized and the circular aperture diameter varies from 0.5λ in (a) to 15λ in (f).

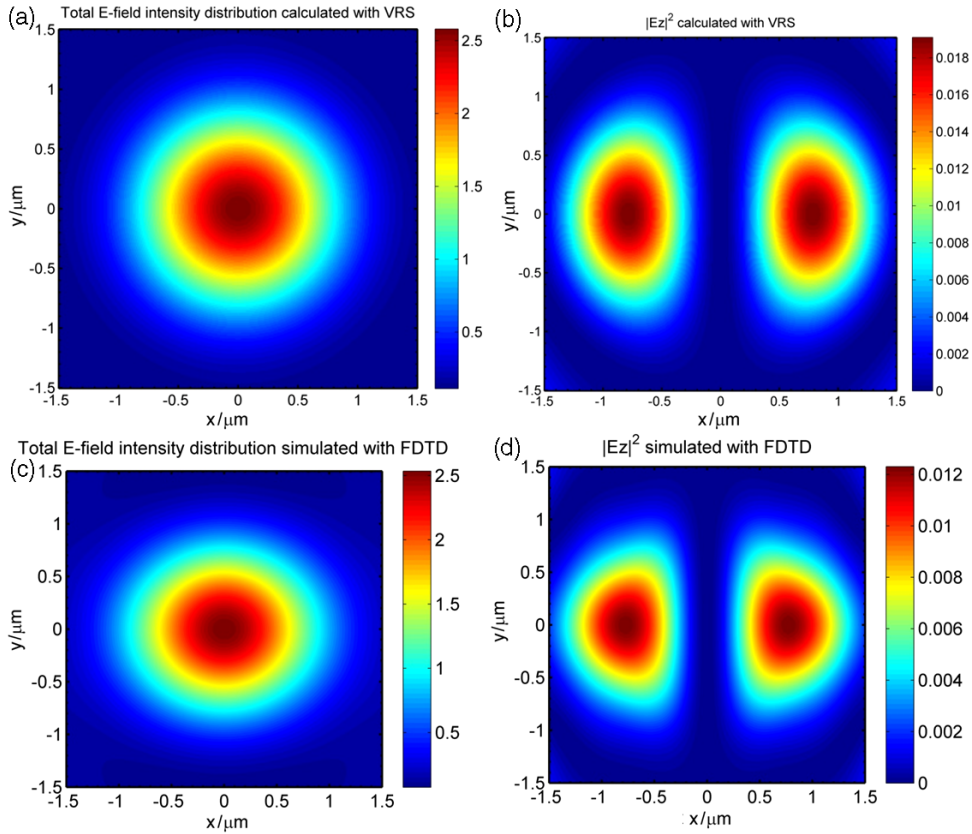


Figure 2. Simulation plots for electric-field distributions at $6.5\ \mu\text{m}$ from a circular aperture with a diameter of 5λ . (a) VRS-computed total E -field intensity. (b) VRS-computed longitudinal E -field intensity. (c) FDTD-computed total E -field intensity. (d) FDTD-computed longitudinal field intensity.

on the symmetry manifested in equations (2a)–(2c). As expected, there is good agreement between the diffraction patterns of figures 2(a) and (c), which are generated by VRS and FDTD, respectively. The same inferences are also evident in the corresponding E -field intensity distributions of the longitudinal component depicted in figures 2(b) and (d). The simulation results of figure 2 indicate that the longitudinal component is much smaller than the transverse

component (whether the numerical results are from VRS or FDTD). However, it may be interpreted from figure 1 that the longitudinal component can instead be dominant with a change of observation plane; we will revisit this issue when considering figure 4 later. Furthermore, we note that the longitudinal component profile is quite different from the profile of total E -field intensity; this is because all of the three mutually orthogonal E -field components will

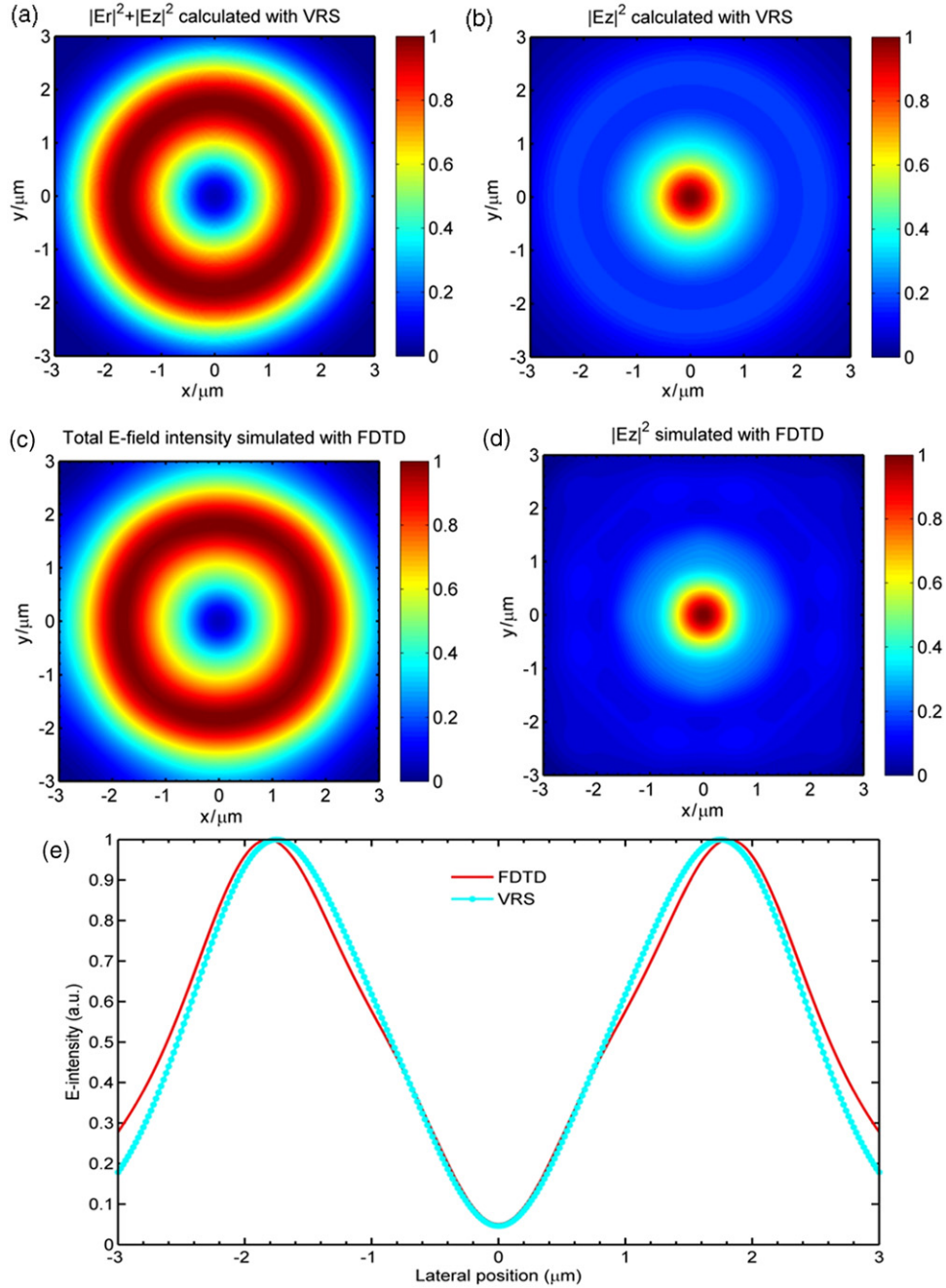


Figure 3. (a), (b) Distribution plots computed by VRS for total E -field intensity and longitudinal E -field intensity, respectively, $10 \mu\text{m}$ away from a circular aperture with $6.4 \mu\text{m}$ diameter when radially polarized light with Gaussian distribution is incident. (c), (d) Distribution plots computed by Lumerical FDTD for total E -field intensity and longitudinal E -field intensity, respectively, $10 \mu\text{m}$ away from same aperture as in (a) and (b). (e) Comparative plots of E -field intensity for (a) and (c).

interfere perfectly at the observation plane due to the vectorial properties of light.

After transforming the first-kind VRS equations into cylindrical coordinates, we find that equation (6a) is, mathematically speaking, the expression for the amplitude E_r of radially polarized light [31, 32]. Both radial and longitudinal components co-exist when the incident light is radially polarized, while only the azimuthal component exists when illuminated by azimuthally polarized light, as seen from equations (6a)–(6c). In our following simulations, incident

light is radially polarized with Gaussian envelope $\exp(-\frac{r^2}{2\omega^2})$, and the other parameter settings are the same except for the polarization change of the incident light. The diameter of the circular aperture is now fixed at 10 wavelengths, and the observation plane is sited $10 \mu\text{m}$ away from the source plane. To provide a common basis for comparison, we chose a radial beam with FWHM = $6 \mu\text{m}$ for both VRS and FDTD simulations. Similar plots of the total E -field intensity profile are observed in figures 3(a) and (c), where the intensity has been normalized so that the total intensity

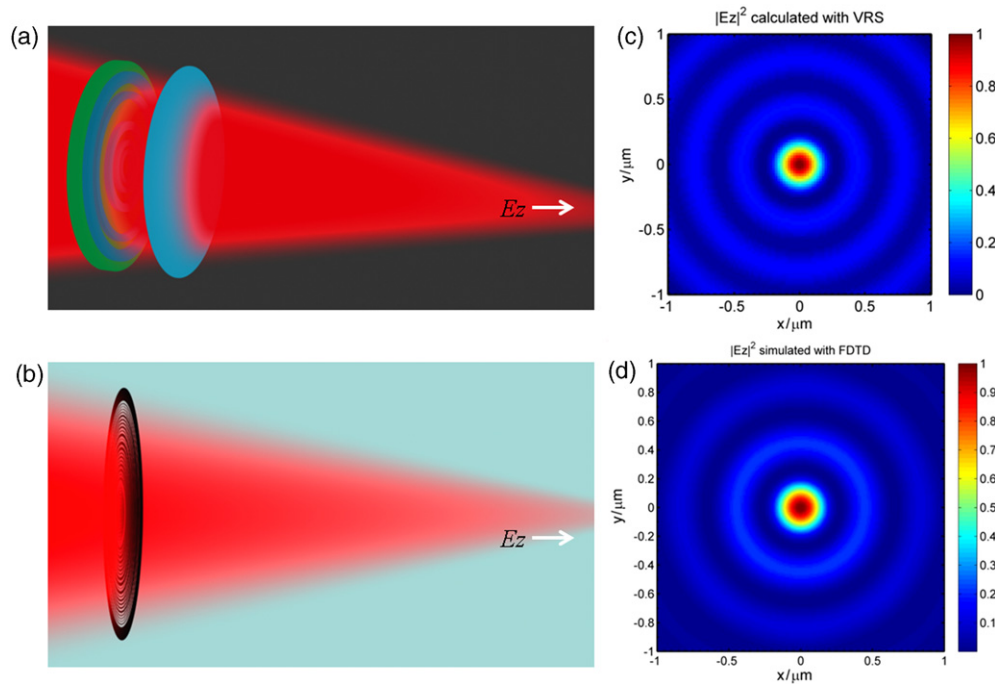


Figure 4. (a) Schematics of a reflection-based lens. (b) Schematics of a planar diffraction-based lens. (c) VRS-computed longitudinal field intensity distributions at an observation plane $10.32 \mu\text{m}$ from the exit side of the film. (d) FDTD-computed longitudinal field intensity distributions at an observation plane $10.32 \mu\text{m}$ from the exit side of the film.

in the focal spot equals one for either case. The same trend is also observed in figures 3(b) and (d) for the corresponding longitudinal component plots. In order to further illustrate the difference between the plots generated by VRS and FDTD, we additionally plot the intensity along the lateral direction in figure 3(e), where we find that the intensity distribution plots are almost coincident. These numerical results help to affirm the validity of VRS for use in the simulation of circular-aperture diffraction problems.

Conventionally, strong and subwavelength longitudinal electric field is realized by a high-NA lens together with a circular or angular aperture [10, 21]. It can be also created by lens-assisted and phase-controlled binary optics [22]. Figure 4(a) depicts schematically how reflection and refraction may be appropriately employed to obtain longitudinally polarized light, utilizing binary optics and a high-NA lens. However, these schemes [10, 21, 22] are quite volumetric and thereby difficult to embed into a contemporary imaging system consisting of highly integrated components. In contrast, our proposed diffraction-based lens in figure 4(b) only relies on planarized ultra-thin concentric rings, thus enabling easy and high-level integration with existing modern complex imaging systems. Moreover, note that far-field super-resolution without a sideband is achieved.

To design such an ultra-thin planar lens, the optical mask is divided into 29 concentric annuli with either zero or unit transmittance, corresponding to metal or air. BPSO (binary particle swarm optimization [26]) is adopted and facilitated drastically by VRS to search for the optimal parameters globally. The objective is to find optimal radii for the creation of a strong and subwavelength longitudinally

polarized hotspot while maintaining low sidelobes (a huge sidelobe is generally inevitable in a super-oscillatory lens [3, 23]). Table 1 lists the optimal diameters and widths of the 29 rings, with the outermost ring having a diameter of $59.4 \mu\text{m}$. Radially polarized light with wavelength $\lambda = 632.8 \text{ nm}$ and a Gaussian envelope is incident, with the observation (imaging) plane $10.32 \mu\text{m}$ away from the exit side of the ultra-thin film. Along the lateral direction, we observe similar profiles from both first-kind VRS and FDTD, with well-matched hotspots. The FWHM of the longitudinal component is calculated as $\text{FWHM} = 0.39\lambda$ in air. Note that such a subwavelength hotspot is focused in the true far-field without resorting to evanescent waves limited to the near-field only.

For the longitudinal E -field intensity profiles in the observation plane, we note from figures 4(c) and (d) that the intensity in the central hotspot is obviously much larger than that of the sidelobes. This is very important for practical imaging applications. This is markedly different from the super-oscillatory lens introduced in [3], where a hotspot with $\text{FWHM} = 0.29\lambda$ is produced in oil (i.e., solid immersion lens). It is still challenging to image an arbitrary object which might touch the region of the sidelobe. It should be pointed out that a hotspot with infinitely small FWHM could be achieved in principle by selecting a different optimization objective. However, this would again fall into the category of a super-oscillatory lens [3] and most energy would be distributed into the sidelobes.

Therefore, it is more physical and meaningful to set the objective function such that the sidelobe is much lower than the central intensity. In this connection, the design parameters are optimized, as shown in table 1, so that most

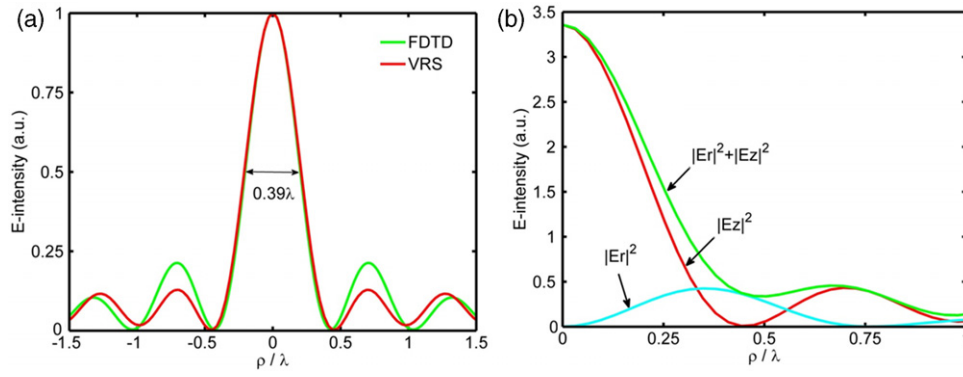


Figure 5. (a) Longitudinal electric-field intensity distributions along the lateral dimension at the observation plane. (b) Electric-field intensity profiles of the radial, longitudinal and total fields along the transverse dimension at the observation plane.

Table 1. Inner and outer radii of the transparent angular regions in the proposed ultra-thin planar lens.

No.	Inner radius (μm)	Outer radius (μm)	No.	Inner radius (μm)	Outer radius (μm)	No.	Inner radius (μm)	Outer radius (μm)
1	0.15	0.8	11	10.55	11.2	21	22	22.65
2	1.3	1.95	12	11.9	12.55	22	23.05	23.7
3	2.45	3.1	13	13.2	13.85	23	24	24.65
4	3.3	3.95	14	14.15	14.8	24	24.95	25.6
5	4.25	4.9	15	15.25	15.9	25	26	26.65
6	5.35	6	16	16.2	16.85	26	26.8	27.45
7	6.2	6.85	17	17.6	18.25	27	27.55	28.2
8	7	7.65	18	19.05	19.7	28	28.25	28.9
9	8.35	9	19	19.8	20.45	29	29.05	29.7
10	9.65	10.3	20	21.15	21.8			

energy is distributed in the subwavelength hotspot with a strong longitudinally polarized component, as observed in figure 5(a). The advantages over using 3D FDTD in the optimization of such a diffraction-based lens are evident in terms of computational time and memory requirement. In figure 5(a), the plots for the transverse and longitudinal field components generated by the proposed VRS agree well with those by numerical results based on FDTD, but at a significantly reduced cost, making robust and efficient optimization attainable in turn. In addition, we note from figure 5(b) that the longitudinal component of the hotspot is dominant in the observation plane.

For our own FDTD example, a single simulation experiment required some 4 h of intensive computation on a Dell Precision T7600 ($2 \times$ Intel Xeon E5-2687w, 256 GB RAM, 3.1 GHz) with the mesh size set at $20 \text{ nm} \times 20 \text{ nm} \times 25 \text{ nm}$. In contrast, use of first-kind VRS allows us to simplify the 3D problem conveniently into a 2D problem along the plane perpendicular to the source plane or even a 1D problem along the optical axis due to axial symmetry; under such circumstances, the task takes only several minutes on any common computer (Intel Core2 Duo, 8 GB RAM, 3.16 GHz). Furthermore, first-kind VRS permits us to focus the simulations on a small region of particular interest (such as a region with a size of $1 \mu\text{m} \times 1 \mu\text{m}$). To ease the computational difficulties in designing and optimizing a diffraction-based lens, the radial coordinate should be divided into N concentric annuli with either unit or zero transmittance;

first-kind VRS together with BPSO may be readily adopted to optimize any flat masks. Such a process can be effectively employed to design lenses meeting optimization objectives such as low noise level, broad field of view or small hotspot size.

4. Conclusion

In conclusion, we have found that a planar diffraction-based lens may be used to generate a subwavelength hotspot with a strong longitudinal electric component ($\text{FWHM} = 0.39\lambda$ in air) for possible application in particle acceleration or high-density data storage with phase-change materials. Consisting of concentric annuli, a planar diffraction-based lens can be readily designed and optimized by use of first-kind vectorial Rayleigh–Sommerfeld integrals. The validity of our proposed approach to analyze aperture diffraction problems has been affirmed by comparison with numerical results obtained by commercially-available FDTD software in all cases of investigation for various and complex polarization states for the thin multi-annulus lens. Due to the significant advantages of VRS over 3D FDTD (accuracy, reliability and computational cost), this research unveils the potential of more efficient design and optimization of a planar diffraction-based lens for a far-field super-resolution hotspot with full polarization control, where the 3D problem can be conveniently simplified into a 2D or even 1D problem along the optical axis.

Acknowledgment

CWQ acknowledges the financial support of the National University of Singapore (project No. R-263-000-688-112).

References

- [1] Ambrosini D and Spagnolo G S 1997 *Am. J. Phys.* **65** 256–7
- [2] Volkov V S, Bozhevolnyi S I and Taillaert D 2004 *Laser Phys. Lett.* **1** 311–6
- [3] Rogers E T F, Lindberg J, Roy T, Savo S, Chad J E, Dennis M R and Zheludev N I 2012 *Nature Mater.* **11** 432–5
- [4] Wolf E and Marchand E W 1964 *J. Opt. Soc. Am.* **54** 587–94
- [5] Heurtley J C 1973 *J. Opt. Soc. Am.* **63** 1003–8
- [6] Southwell W H 1980 *J. Opt. Soc. Am.* **71** 7–14
- [7] Totzeck M 1991 *J. Opt. Soc. Am. A* **8** 27–32
- [8] Gu M 2000 *Advanced Optical Imaging Theory* (New York: Springer)
- [9] Lindfors K, Priimagi A, Setälä T, Shevchenko A, Friberg A T and Kaivola M 2007 *Nature Photon* **1** 228–31
- [10] Dorn R, Quabis S and Leuchs G 2003 *Phys. Rev. Lett.* **91** 233901
- [11] Kotlyar V V and Kovalev A A 2010 *J. Opt. Soc. Am. A* **27** 372–80
- [12] Fischer J and Wegener M 2013 *Laser Photon. Rev.* **7** 22–44
- [13] Duocastella M and Arnold C B 2012 *Laser Photon. Rev.* **6** 607–21
- [14] Lu C and Lipson R H 2010 *Laser Photon. Rev.* **4** 568–80
- [15] Khalil A A I and Sreenivasan N 2005 *Laser Phys. Lett.* **2** 445–51
- [16] Hnatovsky C, Shvedov V, Krolikowshi W and Rode A 2011 *Phys. Rev. Lett.* **106** 123901
- [17] Wuttig M and Yamada N 2007 *Nature Mater.* **6** 824–33
- [18] Lin S K, Lin I C and Tsai D P 2006 *Opt. Express* **14** 4452–8
- [19] Lin S K, Lin I C, Chen S Y, Hsu H W and Tsai D P 2007 *IEEE Trans. Magn.* **43** 861–3
- [20] Tseng M L, Chen B H, Chu C H, Chang C M, Lin W C, Chu N N, Mansuripur M, Liu A Q and Tsai D P 2011 *Opt. Express* **19** 16975–84
- [21] Quabis S, Dorn R, Eberler M, Glockl O and Leuchs G 2000 *Opt. Commun.* **179** 1–7
- [22] Wang H, Shi L, Lukyanchuk B, Sheppard C J R and Chong C T 2008 *Nature Photon* **2** 501–5
- [23] Huang F M and Zheludev N I 2009 *Nano Lett.* **9** 1249–54
- [24] Zhang X and Liu Z 2008 *Nature Mater.* **7** 435–41
- [25] Rho J, Ye Z, Xiong Y, Yin X, Liu Z, Choi H, Bartal G and Zhang X 2010 *Nature Commun.* **1** 143
- [26] Jin N and Rahmat-Samii Y 2007 *IEEE Trans. Antenna Propag.* **55** 556–67
- [27] Lumerical Solutions, Inc. www.lumerical.com
- [28] Luneberg R K 1964 *Mathematical Theory of Optics* (Berkeley, CA: University of California Press)
- [29] Wang H, Sheppard C J R, Ravi K, Ho S T and Vienne G 2012 *Laser Photon. Rev.* **6** 354–92
- [30] Chang C W, Sarychev A K and Shalaev V M 2005 *Laser Phys. Lett.* **2** 351–5
- [31] Fridman M, Machavariani G, Davidson N and Friesem A A 2008 *Appl. Phys. Lett.* **93** 191104
- [32] Xia K G, Ueda K and Li J L 2011 *Laser Phys. Lett.* **8** 354–7